RESEARCH ARTICLE

NANO · MICRO small
www.small-journal.com

# Engineering Hollow-Structured Carbon Framework to Facilitate High-Sulfur-Content Encapsulation for Lithium-Sulfur Batteries

*Jong Hun Sung, Soyun Lee, Jeong-Hoon Yu, Jiwon Lee, Bo Yu, Dong-Hyun Lee, Ha-Young Lee, Seung-Tae Hong, Ibnu Syafiq Imaduddin, Joonhee Kang,* and Jong-Sung Yu**

**Lithium-sulfur batteries (LSBs) have emerged as promising candidates for next-generation energy storage systems due to their high theoretical energy density and cost-effectiveness. However, their practical application is severely limited by the shuttle effect of lithium polysulfides (LiPSs) and the inherently low electrical conductivity of sulfur, which leads to rapid capacity fading and poor rate performance. To address these challenges, this work develops a hollow-structured graphitic nitrogen-doped porous carbon (h-GNPC) framework derived from zeolitic imidazolate framework-8 via a magnesiothermic reduction (MR) process. This method effectively tailors the pore architecture and electrical conductivity, enabling efficient sulfur encapsulation and high sulfur loading up to 90 wt.%. Compared to a carbon host treated without the MR method, the h-GNPC exhibits enhanced porosity, which can accommodate sulfur with stabilized cyclability. As a result, a coin cell with sulfur-loaded h-GNPC cathode exhibits an initial capacity of 1292.9 mAh $g^{-1}$ and enhanced capacity retention of 74.9% over 500 cycles at 0.2 C as well as rate performance. Notably, pouch-type cells assembled with the h-GNPC cathode demonstrate excellent scalability and cycling stability, highlighting the practical potential of this design for the commercialization of LSBs technology.**

## 1. Introduction

The increasing demand for large-scale applications such as electric vehicles and portable electronic devices necessitates high-capacity and high-energy-density energy storage systems.[1–5] At the same time, competition to reduce battery costs is becoming ever more intense, prompting the search for alternatives beyond conventional lithium-ion batteries (LIBs).[6–9] Lithium-sulfur batteries (LSBs) have emerged as one of the most promising next-generation systems due to their exceptionally high theoretical energy density (≈2600 Wh $kg^{-1}$), far surpassing that of current LIBs.[10–16] In addition, sulfur offers several advantages, including low-cost, natural abundance, and environmental benignity.[17–19] Despite these merits, LSBs still suffer from poor cycle performance and limited rate capability, primarily due to the continuous dissolution of lithium polysulfides ($Li_2S_x$, $4 \leq x \leq 8$; LiPSs) intermediates into the electrolyte. Furthermore, the large volumetric expansion of sulfur (≈80% upon lithiation)[20,21] and its intrinsically low electrical conductivity ($5 \times 10^{-30}$ S $cm^{-1}$)[22,23] further degrade battery performance.

To overcome the dissolution and improve the sluggish redox kinetics of LiPSs conversion, many strategies have been suggested such as electrolyte formulations,[24,25] functional separators,[26,27] interlayers,[28,29] and binders.[30,31] In particular, the design of effective sulfur host materials has received considerable attention, as they can physically confine sulfur and chemically adsorb LiPSs, resulting in dramatic improvement on charge–discharge cycle stability of the sulfur electrode.[32] Among various hosts, polar oxides have been traditionally explored as sulfur hosts owing to their strong chemisorption capability for LiPSs intermediates. For example, $La_2O_3$,[33] $TiO_x$,[34] $SiO_2$,[35–37] $CeO_2$,[38] and $MnO_2$[39] have demonstrated notable improvements by suppressing LiPSs dissolution. Similarly, polar (semi)conductive materials including sulfides,[40] phosphides,[41] and nitrides[42–44] have also been investigated as sulfur hosts, offering an alternative to the oxygen-based compounds. However, many of these materials suffer from poor electrical conductivity,

J. H. Sung, J.-H. Yu, J. Lee, B. Yu, D.-H. Lee, H.-Y. Lee, S.-T. Hong, I. S. Imaduddin, J.-S. Yu
Department of Energy Science and Engineering
Daegu Gyeongbuk Institute of Science & Technology (DGIST)
Daegu 42988, Republic of Korea
E-mail: jsyu@dgist.ac.kr

S. Lee, J. Kang
Department of Nano Fusion Technology
Pusan National University
Busan 46241, Republic of Korea
E-mail: j.kang@pusan.ac.kr

H.-Y. Lee, J.-S. Yu
UE Science
R7-507, 333 Techno Jungang-Daero, Daegu 42988, Republic of Korea

The ORCID identification number(s) for the author(s) of this article can be found under https://doi.org/10.1002/smll.202508609



**DOI: 10.1002/smll.202508609**

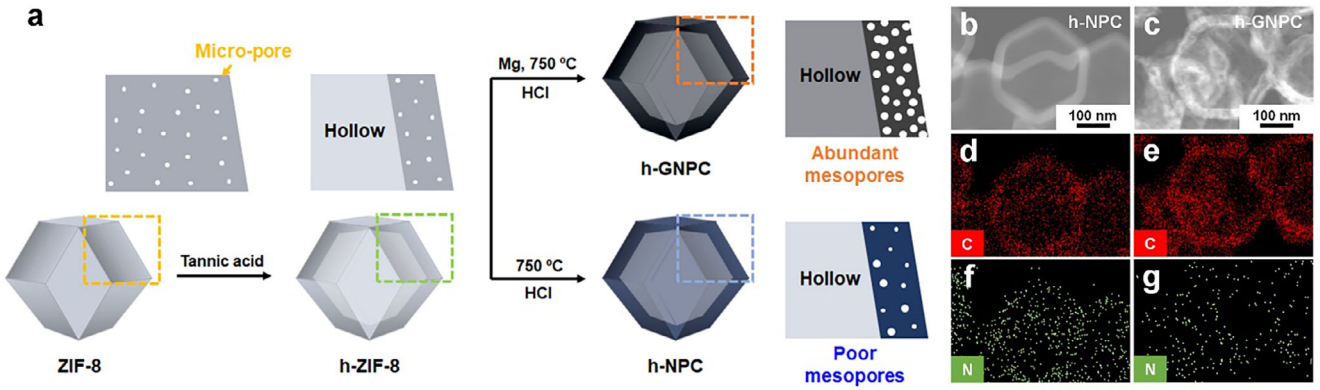


**Figure 1.** a) Schematic representation of host carbon design. b–g) HAADF-STEM and corresponding EDS mapping images for h-NPC and h-GNPC.

which limits their rate performance. This challenge has motivated the use of carbonaceous materials with high surface area and porosity, such as graphene,[23] mesoporous carbon,[45] microporous carbon,[46] metal–organic frameworks (MOFs)-derived carbons.[47] Owing to their excellent electrical conductivity and porous structures, carbonaceous materials are recognized as highly effective sulfur hosts for further improving the performance of the LSBs. Moreover, heteroatom-doped carbons have been widely developed to enhance LiPSs affinity by compensating for the nonpolar nature of conventional carbon surfaces.[48–51] In particular, hollow-structured MOF-derived carbons have shown significant potential in encapsulating sulfur and mitigating LiPSs dissolution via their polar and porous architectures.[52,53] However, many previously reported hollow frameworks exhibit limited pore volume or excessive microporosity in nature, which hinders the diffusion and dense encapsulation of high sulfur content into the hollow interior. Moreover, the hollow MOFs mentioned above generally lack sufficient graphitic property, which plays a crucial role in enhancing electrical conductivity, leading to sluggish electron transport behavior.

Inspired by the synergistic potential of hollow MOF-based structures for LSBs, we propose an innovative design of hollow-structured graphitic nitrogen-doped porous carbon (h-GNPC), synthesized via a magnesiothermic reduction (MR) strategy after selective etching of a zeolitic imidazolate framework-8 (ZIF-8) using tannic acid. The MR treatment not only effectively enlarges the pore size, thereby facilitating the efficient infiltration and uniform dispersion of sulfur within the hollow location, but also significantly enhances the electrical conductivity of the carbon matrix by inducing partial graphitization and forming a graphitic lattice.[54,55] The obtained h-GNPC can accommodate a substantially high sulfur amount (≈90 wt.%) within its hollow area through the engineered pores, as well as exhibit superior rate capability owing to the improved conductivity, while non-MR-treated hollow-structured nitrogen-doped carbon (h-NPC) with insufficient microporous structure cannot easily encapsulate large amount of sulfur, leading to low sulfur utilization. These advantageous features collectively contribute to the realization of long-term cycling performance with a thin (50 µm) lithium metal anode, achieving a capacity retention of 74.9% over 500 cycles at 0.2 C. Furthermore, the electrochemical performance of the h-GNPC-based cathode is successfully validated in a practical pouch-type LSB configuration, which demonstrates a high areal capacity (4.0 mAh $cm^{-2}$) and outstanding capacity retention exceeding 73.0% over 50 cycles, even under commercially relevant conditions of a high sulfur loading (4.4 mg $cm^{-2}$) and a limited electrolyte amount (5.0 µL $mg^{-1}$). As a result, the engineered h-GNPC enables the fabrication of compact electrode with high sulfur loading, thereby offering the potential for higher energy-density in practical LSBs.

## 2. Results and Discussion

The design process of the h-NPC or h-GNPC was illustrated in **Figure 1a**. In brief, h-GNPC was synthesized following the MR method of a hollow-structured zeolitic imidazolate framework (h-ZIF-8) which was designated using zeolitic imidazolate framework (ZIF-8) with a tannic acid (Figure S1, Supporting Information). When Mg metal reacts with h-ZIF-8 under 650 °C as a melting point, the Mg generates magnesium nitride ($Mg_3N_2$) particles by reaction with the C—N bond in the framework. As a result, the nitrogen-deficient reaction results in the formation of a graphitic-like structure. The remaining zinc (Zn) species or $Mg_3N_2$ can be removed by etching with HCl solution. Moreover, the MR serves a hierarchical porous structure in the carbon framework, which tolerates much higher sulfur loading. In addition, the formation of graphiticity originated from the MR also brings the increased electrical conductivity of the h-GNPC. Thus, synergistic controllable porosity with hollow structure and high electronic conductivity can facilitate efficient encapsulation of sulfur in the framework. Both h-NPC and h-GNPC obtained from the parent h-ZIF-8 record similar particle sizes of 350–400 nm in transmission electron microscopy (TEM) (Figure 1b,c; Figure S2, Supporting Information). Interestingly, h-NPC shows a smoother surface with a dense shell, whereas h-GNPC displays a rough surface with a much less dense structure owing to N extraction from h-ZIF-8 during MR process. Corresponding energy-dispersive X-ray spectroscopy (EDS) elemental mapping was performed to investigate the composition of carbon (C) and nitrogen for the h-NPC and h-GNPC samples (Figure 1d–g). The elemental mapping images of the EDS exhibit the homogeneous dispersion of C and N in both samples. As expected, the h-GNPC shows a lower N content than h-NPC (Figure S3, Supporting Information), supporting that the C—N bonding reacts with Mg in the h-ZIF-8 to form $Mg_3N_2$

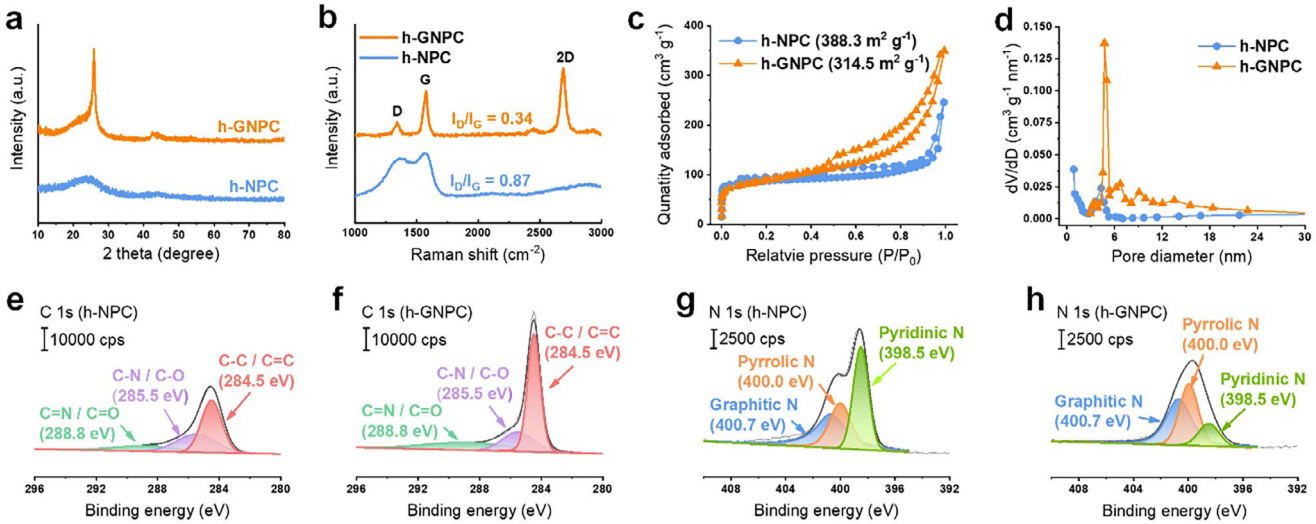


**Figure 2.** a) XRD profiles, b) Raman spectra, c) $N_2$ adsorption-desorption isotherms, and (d) pore size distribution for h-NPC and h-GNPC materials. XPS spectra of e,f) C 1s and g,h) N 1s for h-NPC and h-GNPC.

species. In addition, the Zn signal is not observed in both carbon frameworks (Figures S3 and S4, Supporting Information), displaying complete Zn etching by HCl.

**Figure** 2a exhibits X-ray diffraction (XRD) patterns for both samples treated at 750 °C. The h-GNPC has a distinct diffraction peak ≈26°, assigned to the (002) reflection of graphite, whereas the h-NPC one just shows a broad signal at 25°, which indicates an amorphous carbon.[56] The XRD patterns of parent ZIF-8 and h-ZIF-8 samples are illustrated in Figure S5 (Supporting Information) and the $Mg_3N_2$ presence is confirmed in the h-GNPC before HCl etching (Figure S6, Supporting Information). Raman spectroscopy was employed to differentiate the graphitization degree of the two different carbons (Figure 2b). Two broad peaks were identified at ≈1335 and 1580 $cm^{-1}$. The peak near 1335 $cm^{-1}$, known as the D band, is associated with structural defects and disordered regions containing $sp^3$-hybridized carbon. In contrast, the peak at 1580 $cm^{-1}$, referred to as the G band, corresponds to the C═C bond in graphitic carbon composed of $sp^2$-hybridized carbon atoms. Accordingly, the intensity ratio of the D to G band ($I_D/I_G$) is commonly used to evaluate the level of graphitization. Both samples show Raman bands of G and D, revealing that h-GNPC reveals a lower $I_D/I_G$ intensity ratio of 0.34 with a 2D signal in comparison to that of the h-NPC (0.87) without the 2D peak, emphasizing the former has a higher degree of graphitization, in agreement with the XRD result. In addition, the electrical conductivity of the carbon frameworks was evaluated through a homemade four-probe system, resulting that the h-GNPC has higher electrical conductivity according to graphitization (Figure S7, Supporting Information). Figure 2c,d show $N_2$ adsorption/desorption isotherms and corresponding pore size distribution profiles. The h-NPC shows a coexistence of type I and IV isotherms, resembling those of the parent ZIF-8 and h-ZIF-8 (Figure S8, Supporting Information).[57,58] In contrast, h-GNPC clearly displays standard type IV isotherms with a type H4 hysteresis loop. Moreover, the h-GNPC reveals predominant mesopores with sizes centered at 5 and 15 nm, whereas the h-NPC exhibits micropores with a few mesopores. The information on BET surface area and pore distribution for all samples is summarized in Table S1 (Supporting Information). Figure S9 (Supporting Information) informs that 750 °C is set up as an optimum calcination temperature through confirming the tendency of the graphiticity, morphology, and conductivity of the Mg-treated carbon frameworks under three different temperatures. At a calcination temperature of 650 °C, it is difficult to obtain higher conductivity than that of h-NPC. On the other hand, the h-GNPC sample calcined at 850 °C shows sufficiently increased conductivity and graphitization. However, much higher reactivity between the C—N bond and Mg can be generated at high temperatures, leading to the collapse of the hexagonal structure. Furthermore, the h-GNPC samples were also characterized by varying weight ratio of h-ZIF-8:Mg at fixed temperature of 750 °C (Figure S10, Supporting Information). The h-GNPC exhibits gradually higher graphiticty with the lower $I_D/I_G$ intensity ratio, resulting in increased conductivity. However, similar to the temperature-dependent case, the morphological structure cannot be well-maintained under excessive Mg amount, indicating that the 1:1 (h-ZIF-8:Mg) reveals optimum weight ratio at the 750 °C. X-ray photoelectron spectroscopy (XPS) was performed to confirm the chemical composition of the two carbon frameworks, and all the signals were calibrated by C 1s at 284.5 eV. The C 1s signal in both samples (Figure 2e,f) can be fitted to three individual peaks at 284.5, 285.5, and 288.8 eV, assigned to C—C/C—H, C—N/C—O, and C—N/C═O, respectively. The Mg-treated h-GNPC sample reveals a much stronger C—C peak in comparison to the h-NPC, which is related to graphitic $sp^2$ carbon. Moreover, in general, the N species can be divided into pyridinic, pyrrolic, and graphitic signals, corresponding to binding energies of 398.5, 400.0, and 400.7 eV, respectively.[59,60] As shown in Figure 2g,h, and Figure S11 (Supporting Information), the pyridinic N in the h-NGPC reveals dramatically decreased behavior than that of the h-NPC, while slight increased intensities of the pyrrolic and graphitic N species are observed in h-GNPC.

The sulfur amount was confirmed using a thermogravimetric analysis (TGA) under Ar conditions (**Figure** 3a). Both 90 wt.%

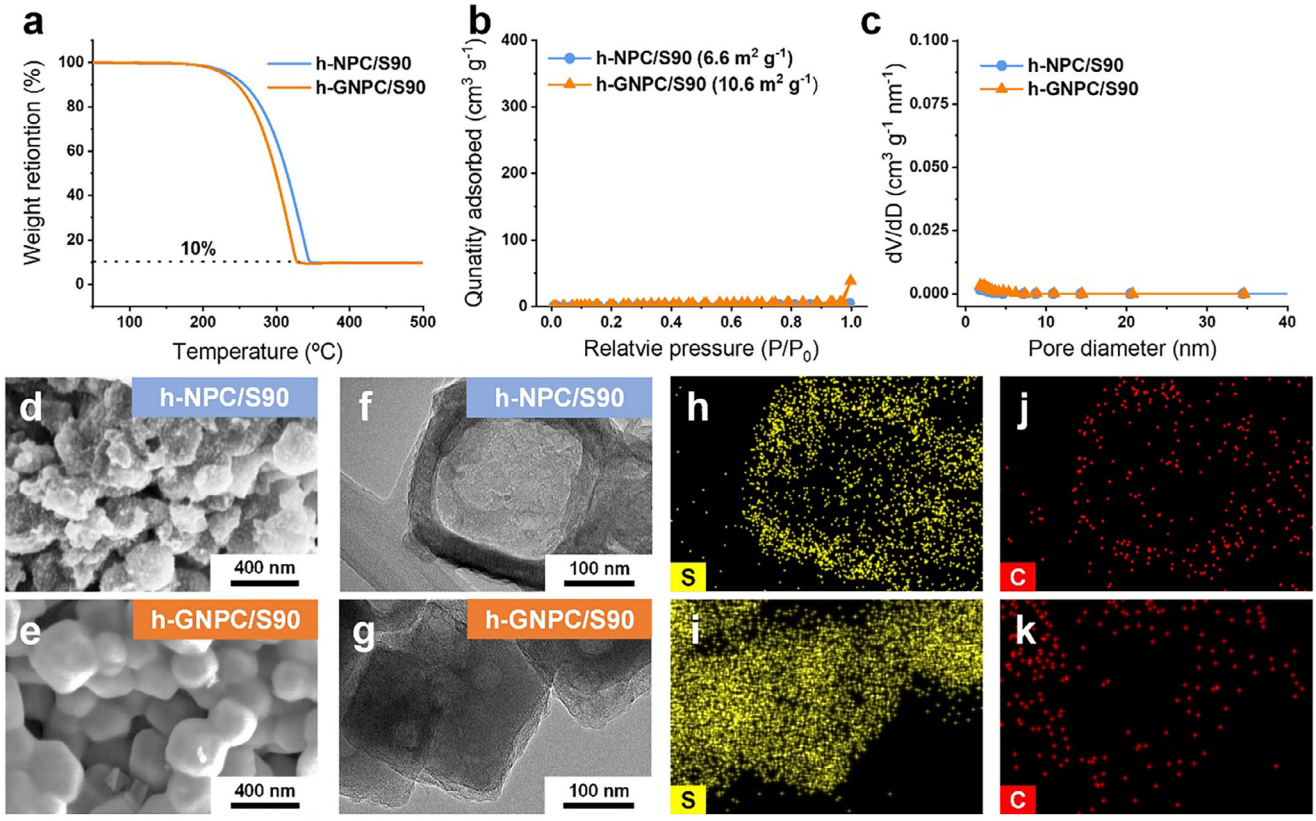


**Figure 3.** a) TGA profiles, b) $N_2$ adsorption-desorption isotherms, c) pore size distribution profiles, and for h-NPC/S90 and h-GNPC/S90 materials. d,e) SEM, f,g) TEM, and h,k) corresponding EDS mapping images for h-NPC/S90 and h-GNPC/S90.

sulfur-loaded h-NPC (h-NPC/S90) and h-GNPC (h-GNPC/S90) result in weight loss up to 90% after 350 °C, in agreement with the sulfur amount. The XRD patterns also support that sulfur is well composed of both carbon hosts (Figure S12, Supporting Information). In addition, both prepared composites exhibit dramatically decreased BET surface area owing to the blocked pores by sulfur loading (Figure 3b,c). The SEM was performed to confirm the morphology of the h-NPC/S90 and h-GNPC/S90 to confirm uniformity of surface (Figure 3d,e). Interestingly, the h-GNPC/S90 displays a much smoother surface like the pristine h-GNPC sample, whereas an uneven and residuary surface is observed in h-NPC/S90. The TEM morphologies and EDS mapping definitely show the sulfur site near the carbon host. In agreement with SEM, the h-GNPC/S90 (Figure 3g,i,k) clearly exhibits well-encapsulated sulfur morphology, whereas the sulfur is located in the frame of the h-NPC particle (Figure 3f,h,j). The schematic illustration of difference between h-NPC/S90 and h-GNPC/S90 is presented in Figure S13 (Supporting Information).

Coin-type cells comprising h-NPC/S90 and h-GNPC/S90 cathodes with the 50 µm Li metal anode were tested under a voltage window of 1.8–2.7 V under defined current density (1 C = 1675 mA $g^{-1}$). The 1st discharge/charge profiles of h-NPC/S90 and h-GNPC/S90 cathodes at 0.2 C are presented in Figure S14a (Supporting Information), achieving discharge capacities of 1095.3 and 1292.9 mAh $g^{-1}$, respectively. Cyclic voltammetry (CV) of the two different cells was also investigated at a scan rate of 0.1 mV $s^{-1}$ (Figure S14b, Supporting Information). The h-NPC/S90 shows the cathodic peaks found at 2.28 and 2.02 V, indicating conversion of solid sulfur ($S_8$) to highly soluble LiPSs and reduction toward insoluble $Li_2S_2/Li_2S$, respectively. In addition, the two anodic peaks found at 2.35 and 2.40 V, corresponding to the transformation from $Li_2S_2/Li_2S$ to soluble LiPSs and oxidation toward solid sulfur, respectively.[61] Interestingly, h-GNPC/S90 reveals the reduction and oxidation peaks at higher (2.29 and 2.07 V) and lower (2.30 and 2.36 V) potentials in comparison to h-NPC/S90, clearly showing enhanced kinetics of the h-GNPC/S90 electrode. The rate capability test was performed by increasing the C-rate from 0.2 to 2 C and then returning to 0.2 C (Figure S15, Supporting Information). The h-GNPC/S90 clearly reveals a higher capacity in comparison to the h-NPC/S90 under at all C-rate stages. Long-term cycle stability test of two prepared cells was further conducted at a C-rate of 0.2 C for 500 cycles (**Figure 4**a). The cell containing h-GNPC/S90 reveals superior retention up to 74.9% (968.3 mAh $g^{-1}$) after 500 cycles, whereas the h-NPC/S90 cell only shows a reversible capacity of 372.9 mAh $g^{-1}$ with a capacity retention of 34.0%. The detailed charge/discharge profiles at different cycles for the long-term cycling are presented in Figure S16 (Supporting Information). The h-GNPC/S90 electrodes, of which h-GNPC were synthesized under different temperatures and h-ZIF-8:Mg ratios conditions, were also tested for 100 cycles at the same current density of 0.2 C. Figure S17 (Supporting Information) supports that the h-GNPC prepared at 750 °C with a weight ratio of 1:1 exhibits much higher cycling performance, in agreement with Figures S9 and S10 (Supporting Information).

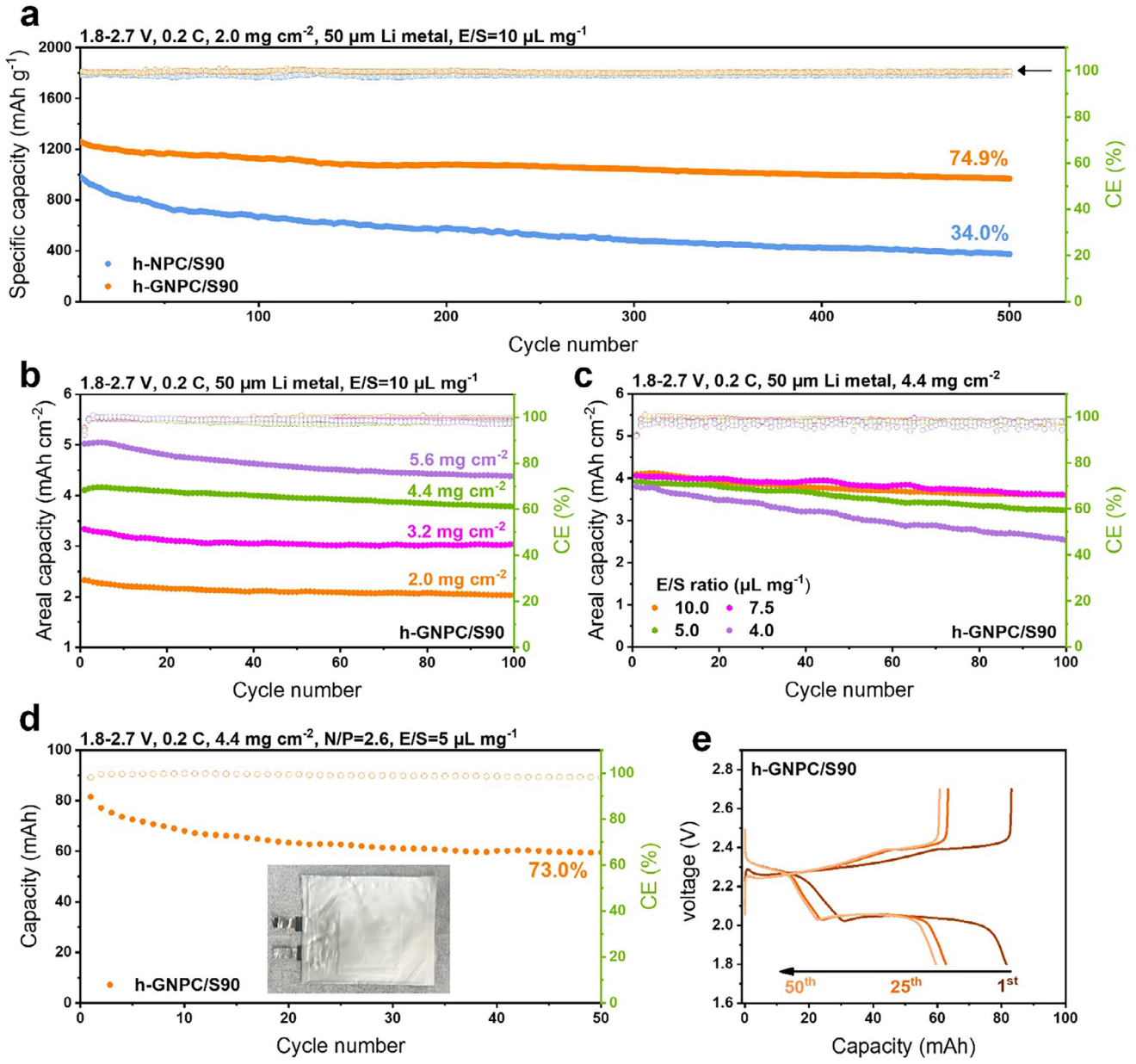


**Figure 4.** Coin-type cell test. a) Cycling performance of h-NPC/90 and h-GNPC/90 cathode under mild conditions of 0.2 C and E/S = 10 μL $mg^{-1}$. Investigation of cycling stability under different b) loadings and c) E/S ratios for h-GNPC cathode. Pouch-type cell test. d) Cycling performance of the cell with h-GNPC cathode and e) corresponding charge/discharge curves at different cycles.

Electrochemical impedance spectroscopy (EIS) was performed before cycling to compare the resistance of two different cells (Figure S18, Supporting Information). The interval between the origin and the initial *x*-axis intercept indicates the electrolyte resistance ($R_s$), attributed to the contact resistance of the electrolyte and electrode under the same electrolyte condition.[36] In addition, the semicircle commonly characterizes the charge transfer resistance ($R_{ct}$), while the linear peak at the low-frequency region can be attributed to Warburg impedance ($W_0$).[62] By using the fitting of the equivalent circuit, the h-GNPC/S90 cell shows a lower calculated $R_{ct}$ of 64.4 Ω in comparison to h-NPC/S90 (92.1 Ω), which is attributed to the much higher conductivity of the h-GNPC host and thus better electrochemical kinetics. Long-term cycling of the h-NPC/S90 and h-GNPC/S90 was further investigated under increased current densities of 1 and 2 C (Figure S19, Supporting Information). It is natural that display decreased cycle performances at higher C-rate, which can be attributed to the intrinsically low electrical conductivity of sulfur and the sluggish redox kinetics of the $Li_2S/Li_2S_x$ conversion.[29,32] Despite these limitations, the h-GNPC/S90 cell reveals relatively well-maintained cyclabilities without cell failure, owing to compensation of the electrical conductivity by the h-GNPC. The thicknesses of the two different cathodes were confirmed through the cross-sectional SEM. Regardless of the same cathode loading, the

lower thickness for the h-GNPC/S90 electrode supports higher energy than that of h-NPC/S90 (Figure S20a,b, Supporting Information). Moreover, the h-GNPC/S90 reveals a well-maintained thickness after 200 cycles, whereas the h-NPC electrode exhibits dramatically expanded behavior (Figure S16c,d, Supporting Information). The excellent cyclability of the h-GNPC/S90 cathode is apparent when compared with previously reported works (Figure S21 and Table S2, Supporting Information). Currently, a much higher cathode loading (> 4.0 mg $cm^{-2}$) with thinner Li metal anode are essential for practical LSBs cells with high energy density.[63,64] It is notable that the cyclability can result in rapid capacity decay when the a higher areal capacity as increasing cathode loading.[65] To confirm stability under the different loading, the h-GNPC/S90 cathodes were investigated under four different loadings for 100 cycles under 0.2 C (Figure 4b). As expected, the h-GNPC/S90 electrodes exhibit gradually higher areal capacity with higher loading. Interestingly, the h-GNPC/S90 cell reveals similar cyclability up to 4.4 mg $cm^{-2}$ with reaching to the areal capacity of 4.0 mAh $cm^{-2}$. In contrast, the h-NPC/S90 cell is unable to achieve 4 mAh $cm^{-2}$ even under 5.6 mg $cm^{-2}$ with resulting in rapid capacity decay (Figure S22, Supporting Information). The h-GNPC/S90 cells were further investigated in different ratios of electrolyte amounts per sulfur mass (E/S, µL $mg^{-1}$) for 100 cycles under optimized loading of 4.4 mg $cm^{-2}$ (Figure 4c). The h-GNPC/S90 cells show similarly stable capacity retentions until the E/S ratio of 5.0 µL $mg^{-1}$. Based on optimized conditions of the h-GNPC host, a pouch-type cell was assembled using 4.4 mg $cm^{-2}$ h-GNPC/S90 cathode (4.0 mAh $cm^{-2}$) and 50 µm Li metal anode (10.5 mAh $cm^{-2}$) with electrolyte of 5.0 µL $mg^{-1}$. The photographs for the prepared electrodes and pouch-type cell are presented in Figure S23 (Supporting Information). Considering the areal capacity of the two electrodes, a capacity ratio of negative electrode to positive electrode (N/P) is approximately calculated to 2.6, revealing superior competitiveness with the N/P condition of recently researched Li metal batteries.[66,67] Energy density of the fabricated pouch-type cell was calculated at the initial cycle and was compared with that of the coin-type cell (Tables S3 and S4, Supporting Information). The coin and pouch cells achieve similar values of 184.5 and 181.7 Wh $kg^{-1}$. Furthermore, the cell with h-GNPC/S90 delivers a capacity retention of 73.0% even over 50 cycles (Figure 4d,e). The SEM images of 50 µm Li metal in the cycled pouch-type cell were also characterized to investigate morphological degradation. As shown in Figure S24 (Supporting Information), slight particle-like growth is found in all cycled electrodes in comparison to a pure one. It is notable that the Li metal exhibits similar morphologies without any dendritic Li growth even after 50 cycles, owing to the use of an imide-based electrolyte with $LiNO_3$ additive, which are well-recognized for stabilizing the Li metal anode.[68,69] These results support that the degradation of Li metal anode can be considered nearly negligible, with cycling performance being predominantly attributed to the cathode. After the 50th cycle, the pouch cell comprising h-GNPC/S90 cathode was then connected to a light-emitting diode (LED). Remarkably, the LED remains in a brightly illuminated state for more than 60 min without noticeable fading (Figure S25, Supporting Information).

The two different carbon hosts were immersed in a LiPSs solution (0.1 M $Li_2S_6$ in 1,2-dimethoxyethane/1,3-dioxolane [DME/DOL]) to characterize the trapping ability. The dark brown color of the $Li_2S_6$ solution displays brightly changed behavior after 12 h, when adding h-NPC and h-GNPC, respectively, meaning that both powders effectively adsorb the LiPSs (**Figure 5a**). In particular, the $Li_2S_6$ solution with h-GNPC is seen to be much more transparent in comparison to that with h-NPC. Ultraviolet-visible (UV–vis) absorption spectroscope was further performed to evaluate the residual $Li_2S_6$ in the two different solutions after 12 h (Figure 5b). The broad peak near 280 nm is observed in all tested solutions, which can be assigned to $S_6^{2-}$ species.[36] Interestingly, the solution containing h-GNPC particles shows lower peak intensity than that with h-NPC, despite the slightly decreased N content in h-GNPC. To further confirm the adsorption of LiPSs in the carbon frameworks, the h-NPC (h-NPC/$Li_2S_6$) and h-GNPC (h-GNPC/$Li_2S_6$) which have been dispersed into the $Li_2S_6$ solution for 12 h and collected after centrifugation were investigated through XPS. For S 2p spectra, both samples show two main $2p_{3/2}$ peaks at 162.1 and 163.1 eV, respectively, which can be attributed to the terminal ($S_T$) and bridging ($S_B$) sulfur atoms, respectively (Figure 5c).[37] Importantly, two mentioned peaks in h-GNPC/$Li_2S_6$ reveal stronger intensity in comparison to the h-NPC/$Li_2S_6$. Two other peaks at 166.7 and 168.2 eV which can be assigned to thiosulfate ($O_3S$-S) and polythionate ($O_3S$-$S_x$-S) are observed in both samples, originating from a few exposures of oxygen in the air.[55] Moreover, the two main peaks at 55.5 and 56.4 eV are fitted in the h-NPC/$Li_2S_6$ and h-GNPC/$Li_2S_6$ samples, corresponding to the Li—S and Li—N bonds for the Li 1s (Figure 5d).[36] In common with S 2p result, the h-GNPC/$Li_2S_6$ shows much stronger intensity than the h-NPC/$Li_2S_6$. Kinetics of $Li_2S$ precipitation on the carbon hosts were examined using chronoamperometric measurements. As shown in Figure 5e, the capacity of $Li_2S$ precipitation for h-GNPC reaches to 220.4 mAh $g^{-1}$ at 2.05 V, revealing higher value in comparison to that for h-NPC (162.1 mAh $g^{-1}$). Moreover, the precipitation of $Li_2S$ for the h-GNPC host ($t$ = 2622 s) occours much faster than on the h-NPC one ($t$ = 2311 s). This finding exhibits that h-GNHPC significantly reduces the $Li_2S$ nucleation overpotential, thereby facilitating the sulfur reduction kinetics.

To examine the influence of nitrogen functionalities on the adsorption behavior of LiPSs species, density functional theory (DFT) calculations were conducted using three different N-doped graphene models. The binding energies of $Li_2S_4$, $Li_2S_6$, and $Li_2S_8$ on each model were calculated according to the following equation:

$$\Delta E_B = E(Substrate) + E\left(Li_2S_x\right) - E\left(Substrate + Li_2S_x\right) \quad (1)$$

The atomic structures of the adsorbed state on the graphene substrates are illustrated in Figure 5f, while the calculated binding energies are summarized in Figure 5g, revealing that the adsorption strength increases in the order of graphitic < pyridinic < pyrrolic, which can be attributed to the local coordination environment of the nitrogen dopant. In particular, pyrrolic N with fewer neighboring carbon bonds exhibits under-coordination, thereby providing much higher active sites for strong interaction with all LiPSs species. Pyridinic N can also exhibit stronger adsorption toward LiPSs owing to its lone pair electrons that enable strong coordination with $Li^+$. Nevertheless, pyrrolic N located at edges or in clustered configurations can provide higher structural flexibility and enhanced local electron density, allowing multiple

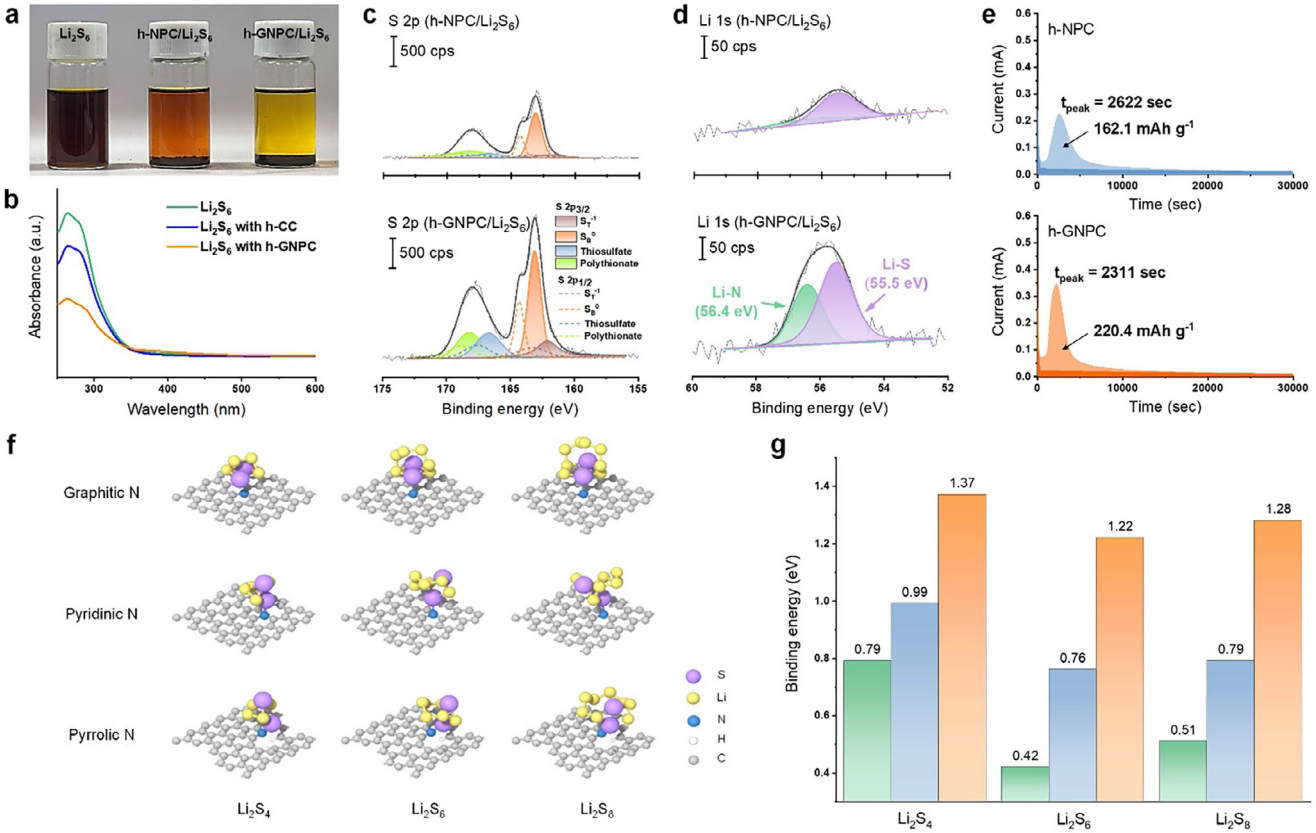


**Figure 5.** a) Digital photograph of $Li_2S_6$ solution and corresponding b) UV–vis adsorption curves of $Li_2S_6$ solution with/without addition of h-NPC or h-GNPC after 12 h. XPS spectra of c) S 2p and d) Li 1s for h-NPC/$Li_2S_6$ and h-GNPC/$Li_2S_6$. e) Potentiostatic discharge curves of h-NPC and h-GNPC electrodes at 2.05 V in $Li_2S_8$-based electrolyte. f) Adsorption structures of N-doped graphene and g) corresponding DFT calculations for binding energies. Green, blue, and orange bars represent the adsorption energies on graphitic, pyridinic, and pyrrolic sites, respectively.

pyrrolic N atoms to simultaneously coordinate with a single Li atom.[70,71] This cooperative multi-coordination effect can in certain cases render pyrrolic N more favorable for anchoring the LiPSs species. This finding is consistent with experimental observations of the h-GNPC, which contains a higher proportion of pyrrolic N. The h-GNPC shows pronounced fading of the $Li_2S_6$ solution in Figure 5a, along with increased sulfur and Li signal intensities in the XPS spectra (Figure 5c,d). These results demonstrate that by tuning the type and proportion of nitrogen functionalities, it is possible to modulate the adsorption strength, providing a viable strategy to suppress the dissolution of LiPSs in the electrolyte.

## 3. Conclusion

In this work, we successfully designed the h-GNPC with hollow structure, polysulfide affinity, and further employed a practical 50 µm Li metal anode for high energy density LSB application. The MR method allows controllable porosity to facilitate the penetration of sulfur into the hollow site of h-GNPC host as well as excellent electrical conductivity. Thereby, the synthesized carbon host with unique morphology and structure enables increased electrochemical properties. For the coin-type cell, the h-GNPC/S90 cathode delivers superior initial capacity (> 1200 mAh $g^{-1}$ at 0.2 C), excellent rate capability at all C-rate values, and remarkable cycling stability (74.9% during 500 cycles) in comparison to the h-NPC/S90 one. Furthermore, the h-GNPC/S90 cathode still exhibits similar capacity retention with that under mild loading and E/S ratio for 100 cycles as well as showing initial capacity of 4.0 mAh $cm^{-2}$, despite increasing the cathode loading and E/S ratio to 4.4 mg $cm^{-2}$ and 5.0 µL $mg^{-1}$, respectively. Aligned with the outstanding performances, the h-GNPC/S90 cathode further shows the possibility for commercialization of the LSBs by exhibiting a well-operated pouch-type cell with 73.0% capacity retention during 50 cycles at extremely practical condition of N/P (2.6) and E/S (5.0 µL $mg^{-1}$) ratios.

## Supporting Information

Supporting Information is available from the Wiley Online Library or from the author.

## Acknowledgements

J.H.S.,S.L., and J.-H.Y. contributed equally to this work. This work was supported by the National Research Foundation (RS-2024-00345686 and RS-2023-00223196) funded by the Korean government. The authors gratefully acknowledge the Korean Basic Science Institutes (KBSI) at Daegu and Pusan as well as the Center for Core Research Facilities (CCRF) in DGIST for providing access to the characterization instruments.

## Conflict of Interest

The authors declare no conflict of interest.

## Data Availability Statement

The data that support the findings of this study are available from the corresponding author upon reasonable request.

## Keywords

carbon, hollow-structure, host, lithium-sulfur batteries, LSBs

Received: July 17, 2025
Revised: September 28, 2025
Published online: October 22, 2025

[1] J. H. Sung, U. H. Lee, J. Lee, B. Yu, M. I. Maulana, S. T. Hong, H. D. Yoo, J. Kang, J. S. Yu, *Adv. Energy Mater.* **2025**, *15*, 2500279.
[2] L. L. Su, N. Yao, Z. Li, C. X. Bi, Z. X. Chen, X. Chen, B. Q. Li, X. Q. Zhang, J. Q. Huang, *Angew. Chem., Int. Ed.* **2024**, *63*, 202318785.
[3] X. Kang, T. He, R. Zou, S. Niu, Y. Ma, F. Zhu, F. Ran, *Small* **2024**, *20*, 2306503.
[4] G. Zhou, H. Chen, Y. Cui, *Nat. Energy* **2022**, *7*, 312.
[5] F. Duffner, N. Kronemeyer, J. Tübke, J. Leker, M. Winter, R. Schmuch, *Nat. Energy* **2021**, *6*, 123.
[6] C. Zhao, G. L. Xu, T. Zhao, K. Amine, *Angew. Chem.* **2020**, *59*, 17634.
[7] W. Xue, Z. Shi, L. Suo, C. Wang, Z. Wang, H. Wang, K. P. So, A. Maurano, D. Yu, Y. Chen, *Nat. Energy* **2019**, *4*, 374.
[8] H. Pan, J. Chen, R. Cao, V. Murugesan, N. N. Rajput, K. S. Han, K. Persson, L. Estevez, M. H. Engelhard, J. G. Zhang, *Nat. Energy* **2017**, *2*, 813.
[9] Z. W. Seh, Y. Sun, Q. Zhang, Y. Cui, *Chem. Soc. Rev.* **2016**, *45*, 5605.
[10] H. J. Peng, J. Q. Huang, X. B. Cheng, Q. Zhang, *Adv. Energy Mater.* **2017**, *7*, 1700260.
[11] D. Bresser, S. Passerini, B. Scrosati, *Chem. Commun.* **2013**, *49*, 10545.
[12] O. Ogoke, G. Wu, X. Wang, A. Casimir, L. Ma, T. Wu, J. Lu, *J. Mater. Chem. A* **2017**, *5*, 448.
[13] S. Zhang, K. Ueno, K. Dokko, M. Watanabe, *Adv. Energy Mater.* **2015**, *5*, 1500117.
[14] P. G. Bruce, S. A. Freunberger, L. J. Hardwick, J. M. Tarascon, *Nat. Mater.* **2012**, *11*, 199.
[15] T. Jin, K. Liang, J. H. Yu, T. Wang, Y. Li, T. D. Li, S. P. Ong, J. S. Yu, Y. Yang, *Nano Lett.* **2024**, *24*, 6625.
[16] H. Raza, S. Bai, J. Cheng, S. Majumder, H. Zhu, Q. Liu, G. Zheng, X. Li, G. Chen, *Electrochem. Energy Rev.* **2023**, *6*, 29.
[17] Y. X. Yin, S. Xin, Y. G. Guo, L. J. Wan, *Angew. Chem., Int. Ed.* **2013**, *52*, 13186.
[18] W. Chen, T. Lei, C. Wu, M. Deng, C. Gong, K. Hu, Y. Ma, L. Dai, W. Lv, W. He, *Adv. Energy Mater.* **2018**, *8*, 1702348.
[19] Z. Huang, P. Jaumaux, B. Sun, X. Guo, D. Zhou, D. Shanmukaraj, M. Armand, T. Rojo, G. Wang, *Electrochem. Energy Rev.* **2023**, *6*, 21.
[20] R. Cao, W. Xu, D. Lv, J. Xiao, J. G. Zhang, *Adv. Energy Mater.* **2015**, *5*, 1402273.
[21] Y. Ansari, S. Zhang, B. Wen, F. Fan, Y. M. Chiang, *Adv. Energy Mater.* **2019**, *9*, 1802213.
[22] F. Pei, T. An, J. Zang, X. Zhao, X. Fang, M. Zheng, Q. Dong, N. Zheng, *Adv. Energy Mater.* **2016**, *6*, 1502539.
[23] X. Jia, C. Zhang, J. Liu, W. Lv, D. W. Wang, Y. Tao, Z. Li, X. Zheng, J. S. Yu, Q. H. Yang, *Nanoscale* **2016**, *8*, 4447.
[24] S. C. Kim, X. Gao, S. L. Liao, H. Su, Y. Chen, W. Zhang, L. C. Greenburg, J. A. Pan, X. Zheng, Y. Ye, *Nat. Commun.* **2024**, *15*, 1268.
[25] Y. Liu, Y. Elias, J. Meng, D. Aurbach, R. Zou, D. Xia, Q. Pang, *Joule* **2021**, *5*, 2323.
[26] R. Razaq, M. M. U. Din, D. R. Småbråten, V. Eyupoglu, S. Janakiram, T. O. Sunde, N. Allahgoli, D. Rettenwander, L. Deng, *Adv. Energy Mater.* **2024**, *14*, 2302897.
[27] J. Zhou, C. Zhang, C. Xie, H. Wang, H. Fan, Y. Guo, C. Wang, F. Chen, Y. Ding, Q. Huang, *Adv. Energy Mater.* **2024**, *14*, 2303063.
[28] Q. Chen, J. Li, J. Pan, T. Li, K. Wang, X. Li, K. Shi, Y. Min, Q. Liu, *Small* **2024**, *20*, 2401153.
[29] S. Yang, D. Jiang, Q. Su, S. Yuan, Y. Guo, K. Duan, M. Xiang, J. Guo, W. Bai, S. Chou, *Adv. Energy Mater.* **2024**, *14*, 2400648.
[30] Z. Liu, X. He, C. Fang, L. E. Camacho-Forero, Y. Zhao, Y. Fu, J. Feng, R. Kostecki, P. B. Balbuena, J. Zhang, *Adv. Funct. Mater.* **2020**, *30*, 2003605.
[31] C. Milroy, A. Manthiram, *Adv. Mater.* **2016**, *28*, 9744.
[32] K. Zhang, Z. Zhao, H. Chen, Y. Pan, B. Niu, D. Long, Y. Zhang, *Small* **2025**, *21*, 2409674.
[33] F. Sun, J. Wang, D. Long, W. Qiao, L. Ling, C. Lv, R. Cai, *J. Mater. Chem. A* **2013**, *1*, 13283.
[34] Z. Li, B. Y. Guan, J. Zhang, X. W. D. Lou, *Joule* **2017**, *1*, 576.
[35] X. Ji, S. Evers, R. Black, L. F. Nazar, *Nat.Commun.* **2011**, *2*, 325.
[36] B. J. Lee, T. H. Kang, H. Y. Lee, J. S. Samdani, Y. Jung, C. Zhang, Z. Yu, G. L. Xu, L. Cheng, S. Byun, Y. M. Lee, K. Amine, J. S. Yu, *Adv. Energy Mater.* **2020**, *10*, 1903934.
[37] B. J. Lee, C. Zhao, J. H. Yu, T. H. Kang, H. Y. Park, J. Kang, Y. Jung, X. Liu, T. Li, W. Xu, X. B. Zuo, G. L. Xu, K. Amine, J. S. Yu, *Nat. Commun.* **2022**, *13*, 4629.
[38] L. Ma, R. Chen, G. Zhu, Y. Hu, Y. Wang, T. Chen, J. Liu, Z. Jin, *ACS Nano* **2017**, *11*, 7274.
[39] X. Liang, C. Y. Kwok, F. Lodi-Marzano, Q. Pang, M. Cuisinier, H. Huang, C. J. Hart, D. Houtarde, K. Kaup, H. Sommer, *Adv. Energy Mater.* **2016**, *6*, 1501636.
[40] J. Zhou, X. Liu, L. Zhu, J. Zhou, Y. Guan, L. Chen, S. Niu, J. Cai, D. Sun, Y. Zhu, *Joule* **2018**, *2*, 2681.
[41] R. Fang, S. Zhao, Z. Sun, D. W. Wang, R. Amal, S. Wang, H. M. Cheng, F. Li, *Energy Storage Mater.* **2018**, *10*, 56.
[42] Z. Sun, J. Zhang, L. Yin, G. Hu, R. Fang, H. M. Cheng, F. Li, *Nat. Commun.* **2017**, *8*, 14627.
[43] Z. Cui, C. Zu, W. Zhou, A. Manthiram, J. B. Goodenough, *Adv. Mater.* **2016**, *28*, 6926.
[44] G. Cao, X. Li, L. Chen, R. Duan, J. Li, Q. Jiang, J. Wang, M. Li, M. Li, J. Wang, *Small* **2024**, *20*, 2311174.
[45] X. Ji, K. T. Lee, L. F. Nazar, *Nat. Mater.* **2009**, *8*, 500.
[46] Z. Li, L. Yuan, Z. Yi, Y. Sun, Y. Liu, Y. Jiang, Y. Shen, Y. Xin, Z. Zhang, Y. Huang, *Adv. Energy Mater.* **2014**, *4*, 1301473.
[47] R. Yan, T. Ma, M. Cheng, X. Tao, Z. Yang, F. Ran, S. Li, B. Yin, C. Cheng, W. Yang, *Adv. Mater.* **2021**, *33*, 2008784.
[48] X. Wang, G. Li, J. Li, Y. Zhang, A. Wook, A. Yu, Z. Chen, *Energy Environ. Sci.* **2016**, *9*, 2533.
[49] Y. Li, G. Chen, J. Mou, Y. Liu, S. Xue, T. Tan, W. Zhong, Q. Deng, T. Li, J. Hu, *Energy Storage Mater.* **2020**, *28*, 196.
[50] X. Zuo, M. Zhen, D. Liu, L. Fu, Y. Qiu, H. Liu, Y. Zhang, *Adv. Funct. Mater.* **2024**, *34*, 2405486.
[51] K. Xiao, J. Wang, Z. Chen, Y. Qian, Z. Liu, L. Zhang, X. Chen, J. Liu, X. Fan, Z. X. Shen, *Small* **2019**, *15*, 1901454.
[52] H. Jiang, X. C. Liu, Y. Wu, Y. Shu, X. Gong, F. S. Ke, H. Deng, *Angew. Chem., Int. Ed.* **2018**, *57*, 3916.
[53] Z. Zhu, Y. Zeng, Z. Pei, D. Luan, X. Wang, X. W. Lou, *Angew. Chem., Int. Ed.* **2023**, *62*, 202305828.
[54] C. H. Shin, H. Y. Lee, C. Gyan-Barimah, J. H. Yu, J. S. Yu, *Chem. Soc. Rev.* **2023**, *52*, 2145.
[55] J. H. Yu, B. J. Lee, S. Zhou, J. H. Sung, C. Zhao, C. H. Shin, B. Yu, G. L. Xu, K. Amine, J. S. Yu, *ACS Nano* **2024**, *18*, 31974.

[56] G. Li, W. Lei, D. Luo, Y. Deng, Z. Deng, D. Wang, A. Yu, Z. Chen, *Energy Environ. Sci.* **2018**, *11*, 2372.
[57] Z. Abbasi, E. Shamsaei, S. K. Leong, B. Ladewig, X. Zhang, H. Wang, *Microporous Mesoporous Mater.* **2016**, *236*, 28.
[58] Q. He, W. Chen, B. Fan, Q. Wei, Y. Zou, *Chem. Eng. J.* **2024**, *496*, 153813.
[59] C. H. Shin, H. Y. Ted, H. Y. Lee, B. J. Lee, S. Kwon, W. A. Goddard III, J. S. Yu, *Appl. Catal. B* **2023**, *334*, 122829.
[60] H. Y. Lee, H. Y. Ted, C. H. Shin, A. Fortunelli, S. G. Ji, Y. Kim, T. H. Kang, B. J. Lee, B. V. Merinov, W. A. Goddard III, C. H. Choi, J. S. Yu, *Appl. Catal. B* **2023**, *323*, 122179.
[61] Z. Shen, X. Jin, J. Tian, M. Li, Y. Yuan, S. Zhang, S. Fang, X. Fan, W. Xu, H. Lu, *Nat. Catal.* **2022**, *5*, 555.
[62] Y. Jia, S. Chen, X. Meng, X. Peng, J. Zhou, J. Zhang, S. Hong, L. Zheng, Z. Wang, C. W. Bielawski, *Small* **2023**, *19*, 2303919.
[63] L. Wang, M. Zhen, Z. Hu, *Chem. Eng. J.* **2023**, *452*, 139344.
[64] S. H. Chung, A. Manthiram, *Joule* **2018**, *2*, 710.
[65] J. Song, T. Xu, M. L. Gordin, P. Zhu, D. Lv, Y. B. Jiang, Y. Chen, Y. Duan, D. Wang, *Adv. Funct. Mater.* **2014**, *24*, 1243.
[66] J. Du, W. Wang, M. Wan, X. Wang, G. Li, Y. Tan, C. Li, S. Tu, Y. Sun, *Adv. Energy Mater.* **2021**, *11*, 2102259.
[67] J. Liu, Z. Bao, Y. Cui, E. J. Dufek, J. B. Goodenough, P. Khalifah, Q. Li, B. Y. Liaw, P. Liu, A. Manthiram, *Nat. Energy* **2019**, *4*, 180.
[68] F. Qiu, X. Li, H. Deng, D. Wang, X. Mu, P. He, H. Zhou, *Adv. Energy Mater.* **2019**, *9*, 1803372.
[69] P. Li, Z. Zhao, Y. Fei, H. Zhang, G. Li, *Adv. Energy Mater.* **2025**, *15*, 2500882.
[70] Y. Gong, W. Ma, Z. Xu, Y. Wang, *New J. Chem.* **2022**, *46*, 12300.
[71] T. Z. Hou, H. J. Peng, J. Q. Huang, Q. Zhang, B. Li, *2D Mater.* **2015**, *2*, 014011.